

# <sup>1</sup> Observability of Ionospheric Space-Time <sup>2</sup> Structure with ISR: A simulation study

John Swoboda,<sup>1</sup> Joshua Semeter,<sup>1</sup> Matthew Zettergren,<sup>2</sup> Philip Erickson,<sup>3</sup>

---

<sup>1</sup>Department of Electrical & Computer

Engineering, Boston University, Boston,  
Massachusetts, USA.

<sup>2</sup>Physical Sciences Department,  
Embry-Riddle Aeronautical University,  
Daytona Beach, Florida, USA.

<sup>3</sup>Haystack Observatory, Massachusetts  
Institute of Technology, Westford,  
Massachusetts, USA.

As with any sensing modality, incoherent scatter radar (ISR) has inherent errors and uncertainty in its measurements. A number of theoretical aspects behind these errors have been documented in the literature. The main sources of this error comes from spatiotemporal ambiguities and statistical errors that arise from the inherent fluctuation of the medium.

From the point of view from an experiment designer these sources of error can lead to a trade off between spatial and temporal resolution and statistical accuracy. The designer then has to work with questions dealing with resource allocation, such as how long to dwell in a specific direction. These questions can be rather hard to solve because there are a large number of degrees of freedom when designing an experiment.

With the recent application of phased array antennas with pulse to pulse steering, the number of degrees of freedom in experiment design have exploded. These types of systems, like AMISR and EISCAT-3D, allow for greater flexibility in processing along with making it is now possible to create full volumetric reconstructions of plasma parameters. These phased array systems are used heavily in the high latitude region of the ionosphere, which can have plasma phenomena that is highly variable in space and time. In order to develop an experiment to observe the plasma phenomena researchers have to wade through a number of different trade offs. To understand all of these trade offs may need to simulate the experiment.

24 This publication will show a simulator that can take a field of plasma pa-  
25 rameters and create ISR data at the IQ level and then process it to show a  
26 possible reconstruction of the parameters field. It can give researchers a new  
27 tool that can assist them in the set up their experiments. To show the util-  
28 ity of the simulator for experiment design for one of the examples we will  
29 data from a self-consistent multi-ionic fluid transport model. This will demon-  
30 strate the impact the forward model of the ISR and give an example of how  
31 to iterate through different simulation set ups.

## 1. Introduction

32 Incoherent scatter radar is an important diagnostic for the ionosphere in that it can  
33 give direct measurements of the intrinsic plasma parameters [*Dougherty and Farley*,  
34 1960; *Farley et al.*, 1961; *Dougherty and Farley*, 1963; *Hagfors*, 1961]. As with all  
35 diagnostic tools it has associated with it sources of errors which include time and  
36 spatial ambiguities [*Farley*, 1969a, b; *Hysell et al.*, 2008; *Swoboda et al.*, 2015].

37 One unique aspect of ISR is that inherent random fluctuations of the plasma are  
38 used to create these measurements. These fluctuations are used by creating second  
39 order statistics from a scattered signal, specifically an autocorrelation function (ACF)  
40 [*Farley*, 1969a]. The statistical nature of the target itself yields the requirement of  
41 averaging numerous realizations of the ACF to reduce the variance of the estimate.  
42 This forces the assumption of stationarity for a space-time cell, which may not be true.  
43 In the end this creates a trade-off between space-time resolution and the variance of  
44 the measurements.

45 Application of electronically steerable array (ESA) technology to ISR has been  
46 a recent advancement for the community. ISRs such as these, like the Advanced  
47 Modular Incoherent Scatter (AMISR) systems, have already been deployed in Poker  
48 Flat Alaska and Resolute Bay Canada [*Nicolls and Heinzelman*, 2007; *Dahlgren et al.*,  
49 2012a]. These ESA based systems are seen as the future of the ISR sensor modality  
50 due to the flexibility in beam steering, processing and other aspects over dish based  
51 systems. The next step in the evolution of these systems is expected to be the  
52 EISCAT-3D project, which will have a number of enhancements such as multi-static

53 processing capability and be able to receive and process data from each phased array  
54 element by default.

55 One benefit of ESA based ISR is that volumetric reconstructions of plasma param-  
56 eters can be created [*Semeter et al.*, 2009; *Nicolls and Heinselman*, 2007; *Dahlgren*  
57 *et al.*, 2012a]. These systems also have been used to reconstruct full vector parameters  
58 using estimates of the ion velocity which can be determined using the Doppler shift  
59 of spectra [*Butler et al.*, 2010; *Nicolls et al.*, 2014]. Still it has been shown that the  
60 volumetric reconstructions can yield measurements with a high degree of ambiguity  
61 [*Dahlgren et al.*, 2012b]. Similar type of ambiguities have been seen when using sys-  
62 tems with a dish antenna as well. In *Semeter et al.* [2005] the authors show an  
63 undersampling in the horizontal dimension, but are able to compensate by changing  
64 processing parameters.

65 With these new capabilities for the ISR community a discussion of the possible  
66 sources of uncertainty and error is needed. These sources of error and ambiguity  
67 though are difficult understand in the context of experiment design. With that in  
68 mind it may be useful to simulate the ISR measurement process before an experiment  
69 is attempted. With that in mind this paper will show how one could simulate an  
70 experiment, the outline of this is as follows. After listing the possible sources of  
71 error and ambiguity in ISR our simulation method will be detailed. After which  
72 a number of examples of the simulator will be shown. These examples range from  
73 a stationary column of enhanced electron density to the output of a self-consistent  
74 multi-fluid ionospheric model [*Zettergren and Semeter*, 2012]. These examples will

75 illustrate how one could develop their experiments in a systematic way in order make  
76 measurements that best reflect the physics present in the ionosphere.

## 2. ISR Errors

77 In this section the main sources of ISR errors will be discussed. The first part  
78 of this discussion will cover the statistical errors that arise from the ISR process.  
79 After that the errors from the spatial and temporal ambiguity of ISR systems will be  
80 shown. This in the end will lead to trade offs that the experiment designer will have  
81 to face.

### 2.1. Statistical Errors

82 To measure the plasma parameters ISR takes advantage of the random fluctuations  
83 of electron density in the ionosphere. The theory of how the plasma parameters  
84 impact the statistics of these fluctuations have been discussed since the first use of  
85 this sensor modality [Gordon, 1958; Dougherty and Farley, 1960; Farley et al., 1961;  
86 Dougherty and Farley, 1963; Hagfors, 1961], and even as recent as 2011 there have  
87 been new formulations of this theory [Kudeki and Milla, 2011; Milla and Kudeki,  
88 2011].

89 The two main sources of statistical error will covered here are the random fluctu-  
90 ations from the electron density and noise from within the sensor itself. There are  
91 other sources of statistical error including sky noise and coherent scatter from other  
92 targets.

93 The raw incoherent scatter signal is itself is a random process. As such it is  
 94 necessary to average samples of an estimator for autocorrelation or spectrum [Diaz  
 95 *et al.*, 2008]. An easy rule of thumb to understand how the error will reduce can be  
 96 seen in *Farley* [1969a],

$$\left\langle \left| \hat{R}(\tau) - R(\tau) \right|^2 \right\rangle \propto \frac{1}{\sqrt{J}}, \quad (1)$$

97 where  $R(\tau)$  is the ACF as a function of lag  $\tau$ ,  $\hat{R}(\tau)$  is its estimate and  $J$  is the number  
 98 of samples or pulses averaged together to create the estimate.

99 The variance of this signal is further degraded once noise from the sensor is added.  
 100 The noise from the sensor is assumed to be uncorrelated to the signal. Thus the error  
 101 from the noise can simply be added to the error from the inherent fluctuations in the  
 102 signal.

## 2.2. Space-Time Errors

103 The errors created through the ambiguity function lead to a blurring or averaging  
 104 of ACFs from different points in time and space. This is similar to a blurring operator  
 105 one might see in a camera or numerous other types of sensors. With ISR this can be  
 106 more problematic due to the non-linear fitting step.

107 The space-time ambiguity,  $L(\tau_s, \mathbf{r}_s, t_s, \tau, \mathbf{r}, t)$ , is the kernel of Fredholm integral  
 108 equation of the first kind operating on the ACF,  $R(\tau, \mathbf{r}, t)$ , which can change over  
 109 space,  $\mathbf{r}$ , and time  $t$ . which can be represented as follows,

$$\rho(\tau_s, \mathbf{r}_s, t_s) = \int L(\tau_s, \mathbf{r}_s, t_s, \tau, \mathbf{r}, t) R(\tau, \mathbf{r}, t) dV dt d\tau, \quad (2)$$

where the subscript  $s$  represents the same variable but now discretely sampled by the radar.

The kernel is a separable function when the spatial coordinates are spherical, where  $(r, \theta, \phi)$  represent, range, azimuth and elevation respectively. This changes Equation 2 as follows,

$$\rho(\tau_s, \mathbf{r}_s, t_s) = \int G(t_s, t) F(\theta_s, \phi_s, \theta, \phi) W(\tau_s, r_s, \tau, r) R(\tau, \mathbf{r}, t) dV dt d\tau, \quad (3)$$

where  $G(t_s, t)$  is the kernel for the time dimension,  $F(\theta_s, \phi_s, \theta, \phi)$  is radar beam shape which acts as a kernel in azimuth and elevation, and  $W(\tau_s, r_s, \tau, r)$  which is the range ambiguity function which acts as a kernel along range  $r$  and lag  $\tau$ . The derivation of this operator can be seen in *Swoboda et al. [2015]*.

These two sources of error create a significant trade off between statistical variation of the signal and spatial and temporal resolution of the signal. In order to reduce the statistical fluctuations in the signal pulses need to be averaged together. This is necessary even for the case where there is no noise, in a sense the infinite signal to noise ratio (SNR) case. This integration is mainly done over time but can be done over space as well. For phased array systems this mixture of spatial and temporal averaging can be done by averaging together beams. This though will reduce cross range resolution but could possibly improve temporal resolution. It is for this reason

<sub>127</sub> these types of trade offs can best be explored through simulation, which will be  
<sub>128</sub> covered in the following sections.

### 3. Simulator

<sub>129</sub> The following section will detail the processing steps in the ISR simulator. The  
<sub>130</sub> simulator allows one to analyze different experiment scenarios by implementing the  
<sub>131</sub> ISR measurement process with the error from both from both space-time ambiguity  
<sub>132</sub> and the statistical error. The space-time ambiguity is modeled using a coordinate  
<sub>133</sub> transform and the pulse as a windowed and the statistical error is taken into  
<sub>134</sub> account by creating complex shaped Gaussian noise. The first part will detail the  
<sub>135</sub> how filters are created to make the noise. The next one will cover creation of the in-  
<sub>136</sub> phase and quadrature data (IQ data). The last portion will detail the processing used  
<sub>137</sub> to create the estimates of the ACFs, which will also be referred to as lag products.

#### 3.1. Creating Filters

<sub>138</sub> The simulator takes as input a discretized set of ionosphere parameters in Cartesian  
<sub>139</sub> coordinates, which change with time. The first step in the simulator will be from  
<sub>140</sub> each set of parameters an ISR spectrum is calculated, Thus for each point in time  
<sub>141</sub> in space for the simulator there will be an intrinsic ISR spectrum. For details on  
<sub>142</sub> creating these spectra see *Kudeki and Milla* [2011] and *Milla and Kudeki* [2011].

<sub>143</sub> Once the spectra have been created the simulator changes to a spherical coordinate  
<sub>144</sub> system. This coordinate change acts as a linear operator in the spatial dimensions  
<sub>145</sub> as the spectra are weighted and averaged. The weighting in azimuth and elevation

is determined by the antenna beam pattern while the weighting in range is simply just a test of whether the spectra are within the range gate. If there are no spectra within the range gate a nearest neighbor rule is used which selects the closest point in Cartesian space. This method to create the spectra for each point is an acceptable approximation because spatial correlations between the electron density fluctuations will be on the order of the Debye length [Farley, 1969a], which is significantly smaller than the beam width or range gate size. The entire process of the spatial sampling is shown in the simplified diagram in Figure 1.

Once the spectrum at the specific point in range and angle space has been determined, the filter is created. The method to create the filter given a desired spectrum or ACF can be done in a number of ways ?. The current implementation in the simulator creates an infinite impulse filter. The coefficients are determined using the ACF by solving the following set of equations,

$$\begin{bmatrix} R_m(0) & R_m(1) & \cdots & R_m(L-1) \\ R_m(L-1) & R_m(0) & \cdots & R_m(L-2) \\ \vdots & \ddots & & \vdots \\ R_m(1) & R_m(2) & \cdots & R_m(0) \end{bmatrix} \begin{bmatrix} a_1 \\ a_2 \\ \vdots \\ a_L \end{bmatrix} = \begin{bmatrix} R_m(1) \\ R_m(2) \\ \vdots \\ R_m(L) \end{bmatrix} \quad (4)$$

where  $R_m(l)$  are the ACF values,  $L$  is the desired length of the filter, and  $a_i$  are the set of filter coefficients. The filter then takes the form in the frequency domain as the following,

$$H_m(z) = \frac{G}{1 - \sum_{l=1}^L a_l z^{-l}}. \quad (5)$$

<sup>162</sup> The gain term  $G$  is used to make sure the noise is the correct variance. This can be  
<sup>163</sup> calculated as

$$G = \sqrt{\sum_{l=0}^L -a_l R_m(l)}, \quad (6)$$

<sup>164</sup> where  $a_0 = -1$ .

### 3.2. IQ Data Creation

<sup>165</sup> The basic idea behind creating the IQ data is to take a complex white Gaussian  
<sup>166</sup> noise process and shape the spectrum of its output using a filter. As seen in the  
<sup>167</sup> previous subsection, each point in space and time will have a separate noise plant  
<sup>168</sup> and filter which is derived from the plasma and radar parameters parameters, like  
<sup>169</sup> that seen in Figure 2.

<sup>170</sup> The creation of one set of IQ data using a CWGN, ( $w(k) \sim CN(0, \mathbf{I})$ ) can be  
<sup>171</sup> represented as the following:

$$y_m(k) = s(k) [h_m(k) * w(k)], \quad (7)$$

<sup>172</sup> where  $s(k)$  is the pulse shape. The pulse shape acts as a window, as the plasma will  
<sup>173</sup> only reflect energy during the time it is illuminated. The application of this filter is  
<sup>174</sup> actually done in the frequency domain. This is possible because the Discrete Fourier  
<sup>175</sup> Transform (DFT) of a vector of CWGN is also CWGN. The only difference is that  
<sup>176</sup> there is a change in the variance, which is tied to the number of points used in the  
<sup>177</sup> DFT [Kay, 1993]. With this in mind Equation 7 can be implemented as the following,

$$y_m(k) = s(k) \sum_{i=0}^{K-1} e^{j\omega_i k} \left[ \sqrt{S_m(\omega_i | \boldsymbol{\theta})} w(\omega_i) \right], \quad (8)$$

<sup>178</sup> where  $\omega_i$  is the frequency variable,  $w(\omega_i) \sim CN(0, \mathbf{I})$  and  $K$  is the number of points

<sup>179</sup> used for the DFT [*Mitchell and Mcpherson, 1981*].

<sup>180</sup> After the data for each range gate  $y_m(k)$  is created the power of the return is

<sup>181</sup> calculated

$$P_r = \frac{cG\lambda^2}{2(4\pi)^2} \frac{P_t}{R^2} \frac{\sigma_e N_e}{(1 + k^2\lambda_D^2), (1 + k^2\lambda_D^2 + T_r)} \quad (9)$$

<sup>182</sup> where  $P_r$  is the power received,  $c$  is the speed of light,  $G$  is the gain of the antenna,

<sup>183</sup>  $P_t$  is the power of the transmitter,  $\sigma_e$  is the electron radar cross section,  $k$  is the

<sup>184</sup> wavenumber of the radar,  $\lambda_D$  is the Debye length,  $N_e$  is the electron density and  $T_r$

<sup>185</sup> is the electron to ion temperature ratio.

<sup>186</sup> Once the power has been calculated for each range all of the data is delayed and

<sup>187</sup> summed together so as to model the arrival of the radar return at the receive:

$$x(n) = \sum_{m=0}^{M-1} \alpha(m) y_m(n-m), \quad (10)$$

<sup>188</sup> where  $\alpha(m) = \sqrt{P_r(m)}/\hat{\sigma}_y$  and  $\hat{\sigma}_y$  is the estimate of the standard deviation of  $y_m(k)$ .

<sup>189</sup> Lastly, to model the inherent noise in the radar and environment more complex

<sup>190</sup> Gaussian noise is added

$$x_f(n) = x(n) + \sqrt{\frac{k_b T_{sys} B}{2}} w(n), \quad w(n) \sim CN(0, 1) \quad (11)$$

where  $k_b$  is Boltzmann's constant,  $T_{sys}$  is the system temperature and  $B$  is the system bandwidth. A full diagram of the model can be seen in Figure 3.

### 3.3. ACF Estimation

After the IQ data has been created it is processed to create estimates of the ACF at desired points of space. This type of processing has been detailed and analyzed in [Farley, 1969a] and in other publications. This processing follows a flow chart seen in Figure 4.

The lag product formation is an initial estimate of the autocorrelation function.

The sampled I/Q can be represented as  $x(n) \in \mathbb{C}^N$  where  $N$  is the number of samples in an inter pulse period. For each range gate  $m \in 0, 1, \dots, M - 1$  an autocorrelation is estimated for each lag of  $l \in 0, 1, \dots, L - 1$ . To get better statistics this operation is performed for each pulse  $j \in 0, 1, \dots, J - 1$  and then summed over the  $J$  pulses. The entire operation to form the initial estimate of  $\hat{R}(m, l)$  can be seen in Equation 12:

$$\hat{R}(m, l) = \sum_{j=0}^{J-1} x(m - \lfloor l/2 \rfloor, j) x^*(m + \lceil l/2 \rceil, j). \quad (12)$$

The case shown in Equation 12 is a centered lag product, other types of lag products calculations are available but generally a centered product is used. In the centered lag product case range gate index  $m$  and sample index  $n$  can be related by  $m = n - \lfloor L/2 \rfloor$  and the maximum lag and sample relation is  $M = N - \lceil L/2 \rceil$ . This lag product formation is the first step in taking a discrete Wigner Distribution [Cohen, 1995].

This specific type of lag product formation is detailed in [Farley, 1969a] and had been referred to as unbiased. This terminology does differ from what is used in

statistic signal processing literature such as [*Shanmugan and Breipohl, 1988*] where the unbiased autocorrelation function estimate is carried out as so,

$$\hat{R}(m, l) = \frac{1}{L - l} \sum_{j=0}^{J-1} x(m - \lfloor l/2 \rfloor, j) x^*(m + \lceil l/2 \rceil, j). \quad (13)$$

With out the  $\frac{1}{L-l}$  term the estimator will be windowed with a triangular function thus impacting the estimate of the ISR spectrum as this will act as a convolution in the frequency domain. This bias is taken into account in [*Farley, 1969a*] but it is simply wrapped up into the ambiguity function.

Applying a summation rule is generally the next step in creating an estimate of the autocorrelation function. This is done to get a constant range ambiguity across all of the lags for long pulse experiment[*Nygren, 1996*]. It also equalizes the statistics for each lag, as the number of samples for each lag in Equation 13 decreases. An example summation rule for a central product is shown in Figure 5. In the figure the image on the left is a basic representation of an ambiguity function of a long pulse. Its mirrored on the right with red bars which would show the integration area under it so the ambiguity function for each lag will be of equal size in range. There are a number of different summing rule each with their own trade offs [*Nygren, 1996*].

Lastly an estimate of the noise correlation is subtracted out of  $\hat{R}(m, l)$ , which is defined as  $\hat{R}_w(m, l)$ :

$$\hat{R}_w(m, l) = \sum_{j=0}^{J-1} w(m_w - \lfloor l/2 \rfloor, j) w^*(m_w + \lceil l/2 \rceil, j), \quad (14)$$

227 where  $w(n_w)$  is the background noise process of the radar. Often the noise process  
 228 is sampled during a calibration period for the radar when nothing is being emitted.  
 229 The final estimate of the autocorrelation function after the noise subtraction and  
 230 summation rule will be represented by  $\hat{R}_f(m, l)$ .

231 After the final estimation of the spectrum is complete the nonlinear least squares  
 232 fitting takes place to determine the parameters. The basic class of nonlinear least-  
 233 squares problems as seen in [Kay, 1993], are shown in Equation 15,

$$\hat{\mathbf{p}} = \underset{\mathbf{p}}{\operatorname{argmin}} (\mathbf{y} - \boldsymbol{\theta}(\mathbf{p}))^* \boldsymbol{\Sigma}^{-1} (\mathbf{y} - \boldsymbol{\theta}(\mathbf{p})). \quad (15)$$

234 In Equation 15, the data represented as  $\mathbf{y}$  would be the final estimate of the au-  
 235 tocorrelation function  $\hat{R}_f(m, l)$  at a specific range or its spectrum  $\hat{S}_f(m, \omega)$ . The  
 236 parameter vector  $\mathbf{P}$  would be the plasma parameters  $N_e$ ,  $T_e$ ,  $T_i$  and various other  
 237 parameters including ion velocities. The fit function  $\boldsymbol{\theta}$  is the IS spectrum calculated  
 238 from models, such as once seen in [Kudeki and Milla, 2011], smeared by the ambi-  
 239 guity function. In the case of the long pulse the ambiguity can be simply applied  
 240 by multiplying it with the autocorrelation function  $R(l)$ , if the summation rule is  
 241 properly applied.

242 In the past ISR researchers have used the Levenberg-Marquart algorithm to fit  
 243 data [Nikoukar et al., 2008]. This specific iterative algorithm moves the parameter  
 244 vector  $\mathbf{p}$  by a perturbation  $\mathbf{h}$  at each iteration[Gavin, 2013]. Specifically Levenberg-  
 245 Marquart was designed to be a sort of meld between two different methods Gradient

<sup>246</sup> Decent, and Gauss-Newton. The perturbation vector  $\mathbf{h}_{lm}$  can be calculated using the  
<sup>247</sup> following:

$$[\mathbf{J}^T \boldsymbol{\Sigma}^{-1} \mathbf{J}] \mathbf{h}_{lm} = \mathbf{J}^T \boldsymbol{\Sigma}^{-1} (\mathbf{y} - \boldsymbol{\theta}(\mathbf{p})) \quad (16)$$

<sup>248</sup> where  $\mathbf{J}$  is the Jacobian matrix  $\partial\boldsymbol{\theta}/\partial\mathbf{p}$  [Levenberg, 1944; Marquardt, 1963].

<sup>249</sup> Using the covariance matrix from the fitted parameters an overall error estimate  
<sup>250</sup> can be achieved. This matrix is calculated using a numerical approximation to the  
<sup>251</sup> Jacobian matrix that the function uses to determine the solution. The Hessian,  $\mathbf{H}$   
<sup>252</sup> is then calculated by using the Jacobian and then inverted to get the covariance  
<sup>253</sup> matrix. Due to the way the numerical routines solve the problem this matrix must  
<sup>254</sup> be multiplied by the error between the estimated parameters and the data,

$$\boldsymbol{\Sigma}_{\hat{\mathbf{p}}} = \frac{(\mathbf{J}^T \mathbf{J})^{-1} (\mathbf{y} - \boldsymbol{\theta}(\hat{\mathbf{p}}))^* \boldsymbol{\Sigma}^{-1} (\mathbf{y} - \boldsymbol{\theta}(\hat{\mathbf{p}}))}{L - N_p}, \quad (17)$$

<sup>255</sup> where  $N_p$  is the number of parameters being fit. The variances of the parameters  
<sup>256</sup> are then taken as the diagonals of the matrix. Often though the Hessian matrix is  
<sup>257</sup> undefined so it can not be inverted so the error term is then set as a NaN.

#### 4. Simulation Examples

<sup>258</sup> The true utility of the simulator is that a number of aspects of ISR processing can  
<sup>259</sup> be explored. This will be shown in the upcoming examples. The first example will  
<sup>260</sup> show how the simulator can be used for larger statistical studies. The next example  
<sup>261</sup> will use a simple distribution of the ionosphere to show the impact of the forward

262 model of the ISR. Lastly, using the output of a fully consistent multi-fluid ionosphere  
263 model we drive the ISR simulator to show how one can plan possible experiments.

264 It is necessary to understand the statistics from the sensors used in scientific studies.

265 In order to do this a large number of measurements must be taken with the sensor.

266 There are issues with this approach in that the inputs can not be controlled so along  
267 with any random variation that may be found in the sensor the random variation  
268 of the measured process must be included. This issue is especially present within  
269 ISR because the measurement of the plasma parameters comes from the inherent  
270 variation of the plasma density. With the simulator the statistical fluctuations from  
271 only the measurement mechanism only can be studied.

272 To perform a statistical analysis a field of constant plasma parameters is created.

273 The plasma parameter values are listed in Table 1. A large number of statistics can  
274 be built up to create distributions of parameter values like that which can be seen  
275 in Figure 6. These statistics can show the added uncertainty from the measurement  
276 mechanism. This can also be used as a form of boot strapping to determine errors  
277 on measurements in a high fidelity fashion.

278 An important aspect of experiment design is determining the observability of  
279 plasma phenomena with ISR. The simulator can be used to determine the best ex-  
280 periment set up. With this in mind a simple two dimensional field of ionospheric  
281 parameters is constructed to demonstrate this. This O<sup>+</sup> ionosphere is created with a  
282 background electron density that follows a Chapman function with 1e<sup>11</sup> m<sup>-3</sup> as the  
283 peak value and a constant electron and ion temperature. The background electron

284 density can be seen in Figure 7. The spatial sampling pattern can be seen in Figure  
285 8, where each dot is a range gate in one of the 25 beams used.

286 The first set of simulations shows an enhancement moving through the field of view  
287 of the radar. This thin enhancement is 2 km in width and enhances the density by  
288 5 times. The enhancement is at the resolution limit of the original Cartesian grid, a  
289 delta function in the x direction. This can give an idea to how the ISR will blur the  
290 enhancement. This blurring is seen in Figure 9 where the result of the ISR simulation  
291 is shown for runs with a 15 second and 60 second integration time, 60 and 240 pulses  
292 per position respectively. The different integration times show that the variance of  
293 the measurement can impact the quality of the reconstruction because of the inherent  
294 noise quality of the signal.

295 The blurring effect is not constant throughout the space due to the way the radar  
296 samples the space. This is illustrated in Figures 10 and 11, where as the enhancement  
297 moves through the scene its apparent size is affected by the orientation of the radar  
298 beams. As the enhancement becomes parallel to the radar beams then the shape  
299 in the reconstruction becomes smaller along the x-axis. This is because the range  
300 ambiguity is much larger than the cross range ambiguity from the beam pattern.

301 This sort of experiment is continued further by using plasma parameters derived  
302 from a multi-fluid model developed in *Zettergren and Semeter* [2012] to drive the  
303 simulator. The specific example was originally used in *Perry et al.* [2015] to compare  
304 to measurements from RISR-N. Images of the plasma parameters can be seen in  
305 Figures 12 and 13.

306 The output of the ISR simulator from the parameters can be see in Figure 15. This  
307 simulation shows a 60 second integration time, which for the 27 beam experiment  
308 set up gives 255 pulses per position. The depletion in electron density can still be  
309 observed in some of the figures.

310 Also added to show the trade offs between statistical errors and errors cause by  
311 a larger time ambiguity Figure 16 show the fitted parameters after 240 seconds of  
312 integration time or 1021 pulses per position. The last set of images in Figure 17,  
313 show the fitted parameters after 15 seconds of integration or 64 pulses per position.

314 In all cases the depletion is visible. Still as the variance of the measurement is  
315 reduced, i.e. more pulses are integrated the feature is easier to pick out.

## 5. Conclusion

316 Sources of error in the ISR measurement process have be discussed along with the  
317 description of a full simulation of the measurement process. Possible uses for the  
318 simulator in research community have also been discussed and examples have been  
319 show. The simulator can help researchers plan their experiments and help understand  
320 the statistical errors that may arise from their experiments.

321 **Acknowledgments.** This work was supported by the National Science Founda-  
322 tion, through Aeronomy Program Grant AGS-1339500 to Boston University and  
323 Cooperative Agreement AGS-1242204 between the NSF and the Massachusetts In-  
324 stitute of Technology, and by the Air Force Office of Scientific Research under contract  
325 FA9550-12-1-018. The authors are grateful to the International Space Science Insti-

tute (ISSI, Bern, Switzerland) for sponsoring a series of workshops from which the  
idea for this work emerged.

Software used to create figures for this publications can be found at  
<https://github.com/jswoboda/>. Please contact the corresponding author, John Swo-  
boda at swoboj@bu.edu, with any questions regarding the software along with any  
requests for the specific data used for the figures.

## References

- Butler, T. W., J. Semeter, C. J. Heinselman, and M. J. Nicolls (2010), Imaging f  
region drifts using monostatic phased-array incoherent scatter radar, *Radio Sci.*,  
45(5), RS5013, doi:10.1029/2010RS004364.
- Cohen, L. (1995), *Time Frequency Analysis*, Prentice Hall.
- Dahlgren, H., J. L. Semeter, K. Hosokawa, M. J. Nicolls, T. W. Butler, M. G. Johnsen,  
K. Shiokawa, and C. Heinselman (2012a), Direct three-dimensional imaging of polar  
ionospheric structures with the resolute bay incoherent scatter radar, *Geophysical  
Research Letters*, 39(5), doi:10.1029/2012GL050895.
- Dahlgren, H., G. W. Perry, J. L. Semeter, J. P. St. Maurice, K. Hosokawa, M. J.  
Nicolls, M. Greffen, K. Shiokawa, and C. Heinselman (2012b), Space-time variabil-  
ity of polar cap patches: Direct evidence for internal plasma structuring, *Journal  
of Geophysical Research: Space Physics*, 117(A9), doi:10.1029/2012JA017961.
- Diaz, M. A., J. L. Semeter, M. Oppenheim, and M. Zettergren (2008), Particle-in-  
cell simulation of the incoherent scatter radar spectrum, *Radio Science*, 43(1),

- 346 n/a–n/a.
- 347 Dougherty, J. P., and D. T. Farley (1960), A theory of incoherent scattering of  
348 radio waves by a plasma, *Proceedings of the Royal Society of London. Series A,  
349 Mathematical and Physical Sciences*, 259(1296), pp. 79–99.
- 350 Dougherty, J. P., and D. T. Farley (1963), A theory of incoherent scattering of radio  
351 waves by a plasma, 3 scattering in a partly ionized gas, *Journal of Geophysical  
352 Research*, 68, 5473.
- 353 Farley, D. T. (1969a), Incoherent scatter correlation function measurements, *Radio  
354 Sci.*, 4(10), 935–953.
- 355 Farley, D. T. (1969b), Incoherent scatter power measurements; a comparison of var-  
356 ious techniques, *Radio Sci.*, 4(2), 139–142.
- 357 Farley, D. T., J. P. Dougherty, and D. W. Barron (1961), A theory of incoherent  
358 scattering of radio waves by a plasma ii. scattering in a magnetic field, *Proceedings  
359 of the Royal Society of London. Series A, Mathematical and Physical Sciences*,  
360 263(1313), pp. 238–258.
- 361 Gavin, H. P. (2013), The levenberg-marquardt method for nonlinear least squares  
362 curve-fitting problems.
- 363 Gordon, W. (1958), Incoherent scattering of radio waves by free electrons with appli-  
364 cations to space exploration by radar, *Proceedings of the IRE*, 46(11), 1824–1829,  
365 doi:10.1109/JRPROC.1958.286852.
- 366 Hagfors, T. (1961), Density fluctuations in a plasma in a magnetic field, with ap-  
367 plications to the ionosphere, *Journal of Geophysical Research*, 66(6), 1699–1712,

368 doi:10.1029/JZ066i006p01699.

369 Hysell, D. L., F. S. Rodrigues, J. L. Chau, and J. D. Huba (2008), Full profile  
370 incoherent scatter analysis at jicamarca, *Annales Geophysicae*, 26(1), 59–75, doi:  
371 10.5194/angeo-26-59-2008.

372 Kay, S. (1993), *Fundamentals of Statistical Signal Processing, Vol. I - Estimation  
373 Theory*, Prentice Hall.

374 Kudeki, E., and M. Milla (2011), Incoherent scatter spectral theories: Part i: A gen-  
375 eral framework and results for small magnetic aspect angles, *IEEE Transactions on  
376 Geoscience and Remote Sensing*, 49(1), 315–328, doi:10.1109/TGRS.2010.2057252.

377 Levenberg, K. (1944), A method for the solution of certain non-linear problems in  
378 least squares, *Quarterly of Applied Mathematics*, 2, 164–168.

379 Marquardt, D. W. (1963), An algorithm for least-squares estimation of nonlinear  
380 parameters, *Journal of the Society for Industrial and Applied Mathematics*, 11(2),  
381 431–441.

382 Milla, M., and E. Kudeki (2011), Incoherent scatter spectral theories-part ii: Model-  
383 ing the spectrum for modes propagating perpendicular to  $\mathbf{b}$ , *IEEE Transactions on  
384 Geoscience and Remote Sensing*, 49(1), 329–345, doi:10.1109/TGRS.2010.2057253.

385 Mitchell, R., and D. Mcpherson (1981), Generating nonstationary random sequences,  
386 *Aerospace and Electronic Systems, IEEE Transactions on*, AES-17(4), 553–560,  
387 doi:10.1109/TAES.1981.309184.

388 Nicolls, M. J., and C. J. Heinselman (2007), Three-dimensional measurements of  
389 traveling ionospheric disturbances with the Poker Flat Incoherent Scatter Radar,

- 390      *Geophysical Research Letters.*
- 391      Nicolls, M. J., R. Cosgrove, and H. Bahcivan (2014), Estimating the vector electric  
392      field using monostatic, multibeam incoherent scatter radar measurements, *Radio*  
393      *Science*, 49(11), 1124–1139, doi:10.1002/2014RS005519.
- 394      Nikoukar, R., F. Kamalabadi, E. Kudeki, and M. Sulzer (2008), An efficient near-  
395      optimal approach to incoherent scatter radar parameter estimation, *Radio Science*,  
396      43(5), doi:10.1029/2007RS003724.
- 397      Nygren, T. (1996), *Introduction to Incoherent Scatter Measurements*, Invers OY.
- 398      Perry, G. W., H. Dahlgren, M. J. Nicolls, M. Zettergren, J. P. St Maurice, J. L. Seme-  
399      ter, T. Sundberg, K. Hosokawa, K. Shiokawa, and S. Chen (2015), Spatiotemporally  
400      resolved electrodynamic properties of a Sun-aligned arc over Resolute Bay, *Journal*  
401      *of Geophysical Research: Space Physics . . .*, 120(11), 9977–9987.
- 402      Semeter, J., C. J. Heinselman, G. G. Sivjee, H. U. Frey, and J. W. Bonnell (2005),  
403      Ionospheric response to wave-accelerated electrons at the poleward auroral bound-  
404      ary, *Journal of Geophysical Research*, 110(A11), A11,310–13.
- 405      Semeter, J., T. Butler, C. Heinselman, M. Nicolls, J. Kelly, and D. Hamp-  
406      ton (2009), Volumetric imaging of the auroral ionosphere: Initial results from  
407      pfisr, *Journal of Atmospheric and Solar-Terrestrial Physics*, 71, 738 – 743, doi:  
408      10.1016/j.jastp.2008.08.014.
- 409      Shanmugan, K. S., and A. M. Breipohl (1988), *Random Signals Detection Estimation*  
410      *and Data Analysis*, first ed., Wiley.

<sub>411</sub> Swoboda, J., J. Semeter, and P. Erickson (2015), Space-time ambiguity functions  
<sub>412</sub> for electronically scanned isr applications, *Radio Science*, 50(5), 415–430, doi:  
<sub>413</sub> 10.1002/2014RS005620.

<sub>414</sub> Zettergren, M., and J. Semeter (2012), Ionospheric plasma transport and loss in  
<sub>415</sub> auroral downward current regions, *J. Geophys. Res.*, 117(A6), A06,306, doi:  
<sub>416</sub> 10.1029/2012JA017637.

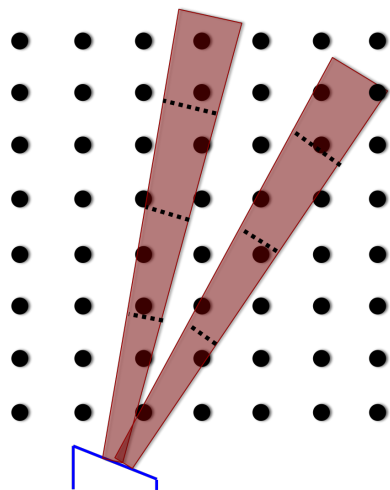


**Figure 1.** Beam Sampling Diagram

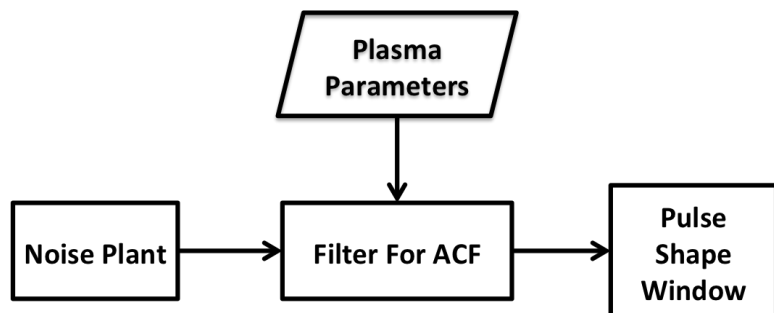


**Figure 2.** Diagram for I/Q simulator signal flow.

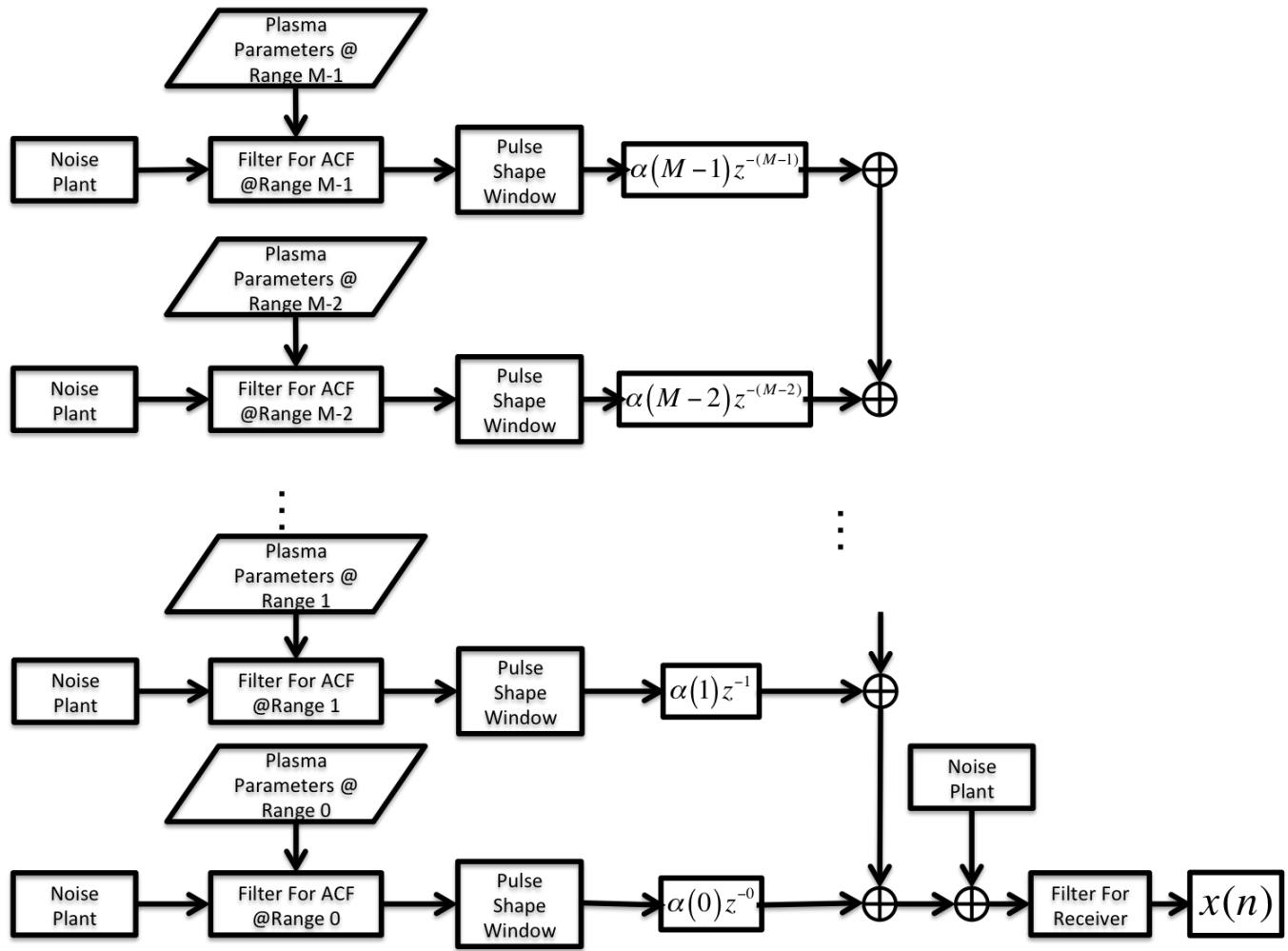
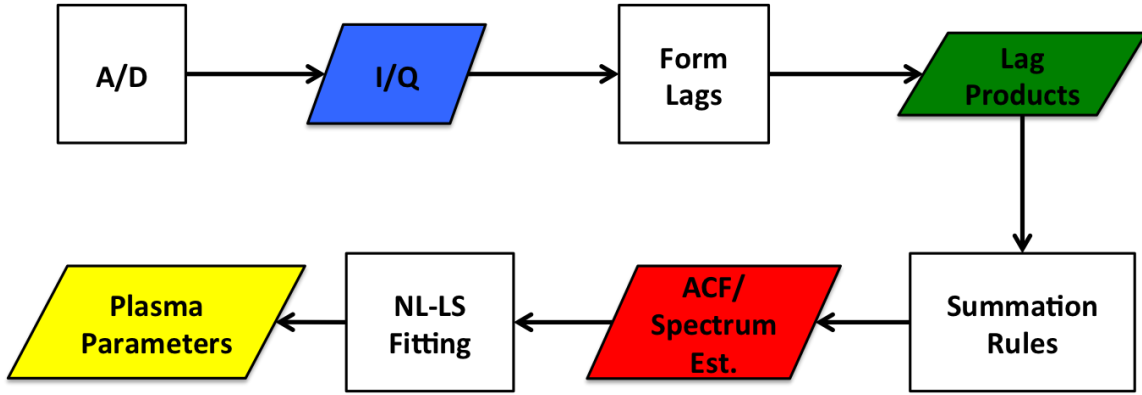
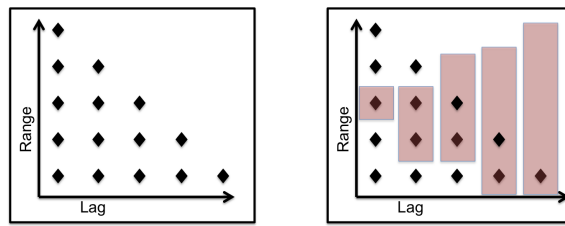


Figure 3. ISR Simulation Diagram



**Figure 4.** ISR signal processing chain, with signal processing operations as squares and data products as diamonds.



**Figure 5.** Summation Rule Diagram

**Table 1.** Simulation parameters.

Species	O+ e-
$N_e$	$1e11$
$T_e$	$2500^\circ \text{ K}$
$T_i$	$2500^\circ \text{ K}$
$V_i$	0 m/s

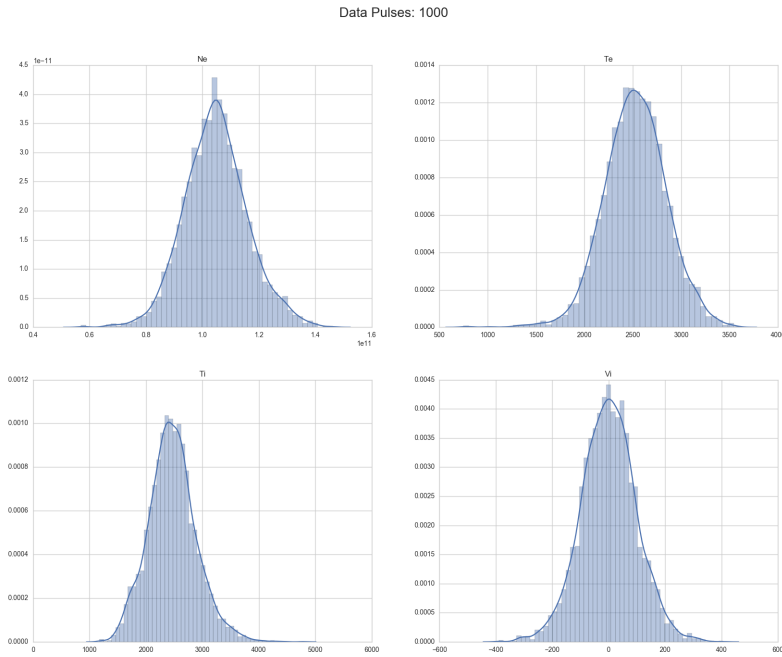


**Figure 6.** Distribution of fitted plasma measurements from cases with 1000 pulses

integrated. The bars are histograms and the blue lines Gaussian Kernel Density estimate of the distribution.

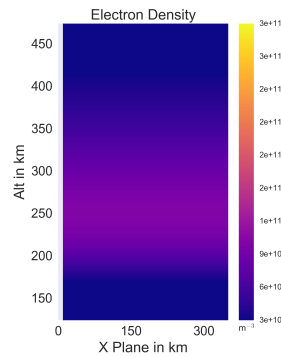


**Figure 7.** Contour of background  $N_e$  simulations.

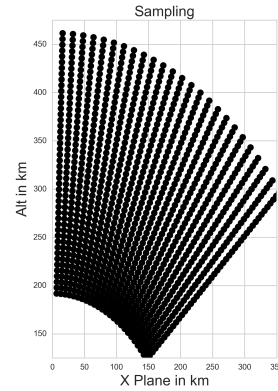


**Figure 8.** Spatial sampling pattern for ISR.

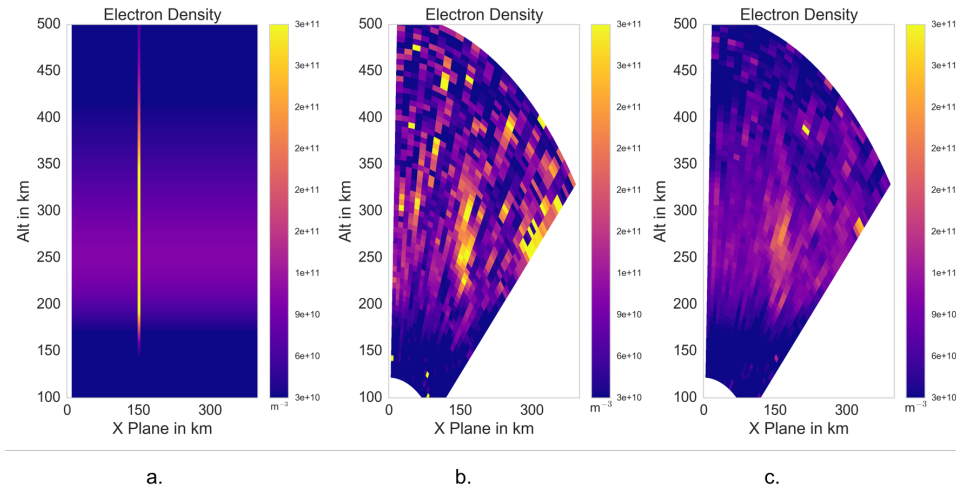


**Figure 9.** Results of stationary enhancement simulation. a. Input  $N_e$ ; b. Output of simulator with 15 second integration; Output of simulator with 60 second integration.

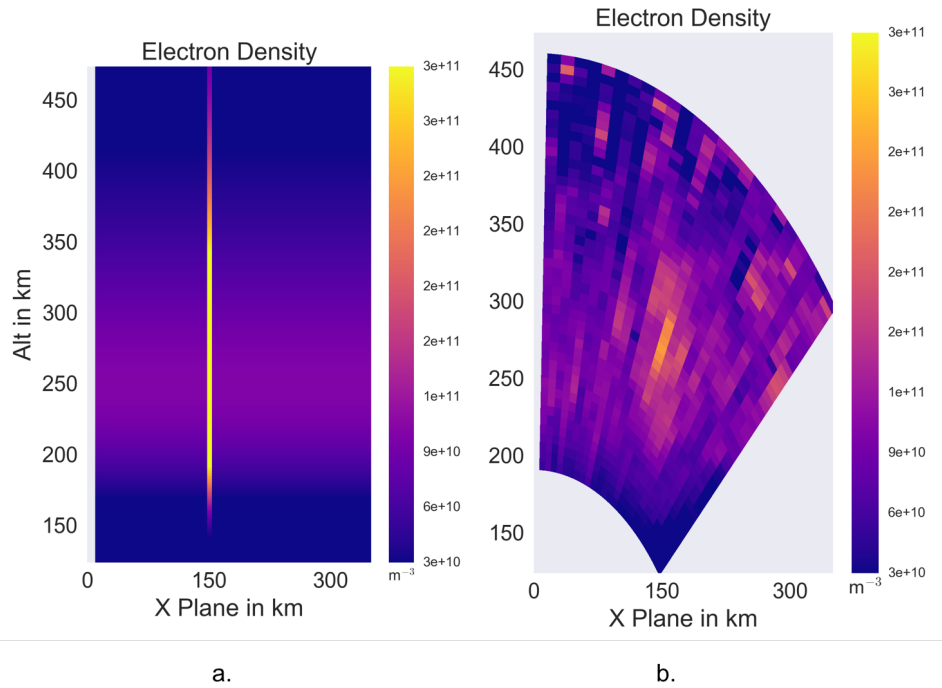


**Figure 10.** Results of moving enhancement simulation at 600 seconds. a. Input  $N_e$ ; b. Output of simulator with 60 second integration.

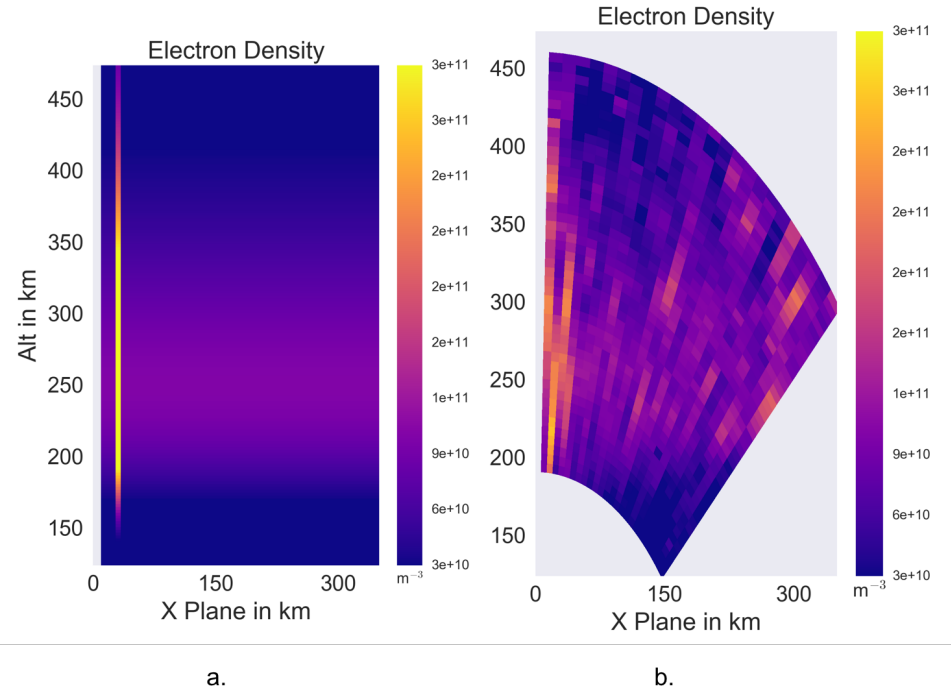


**Figure 11.** Results of moving enhancement simulation at 840 seconds. a. Input  $N_e$ ; b. Output of simulator with 60 second integration.

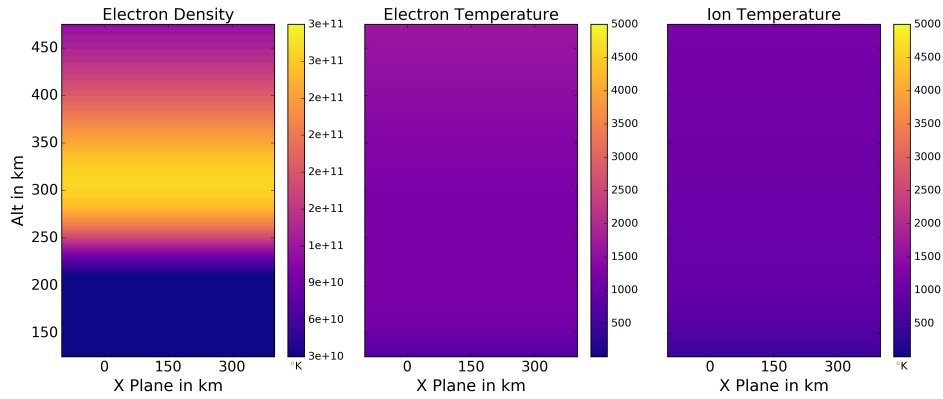


**Figure 12.** Contour of background ionospheric parameters ( $N_e$ ,  $T_e$ ,  $T_i$ ) used for simulations.

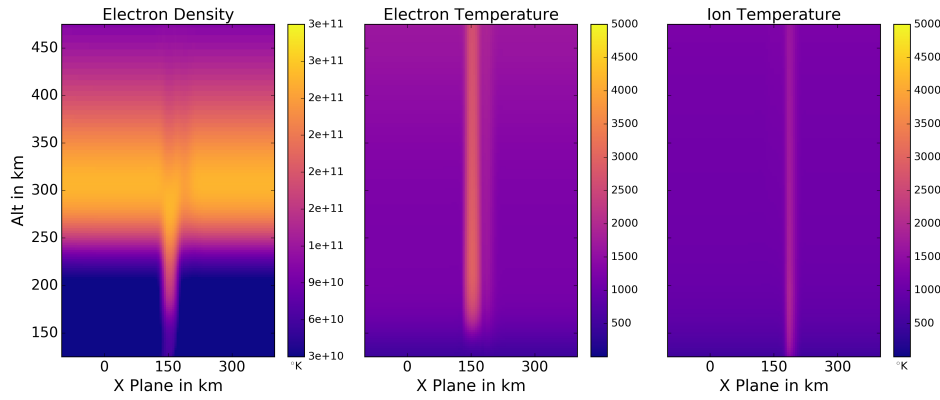


**Figure 13.** Perturbations to Figure 12 due to an imposed current system of .875  $\mu\text{A}/\text{m}^2$  at  $t = 480$  s.

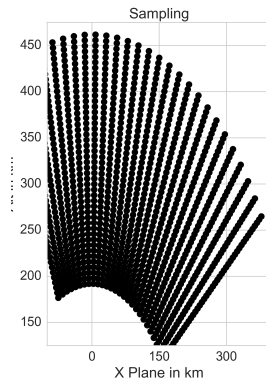


**Figure 14.** Spatial sampling pattern for ISR.

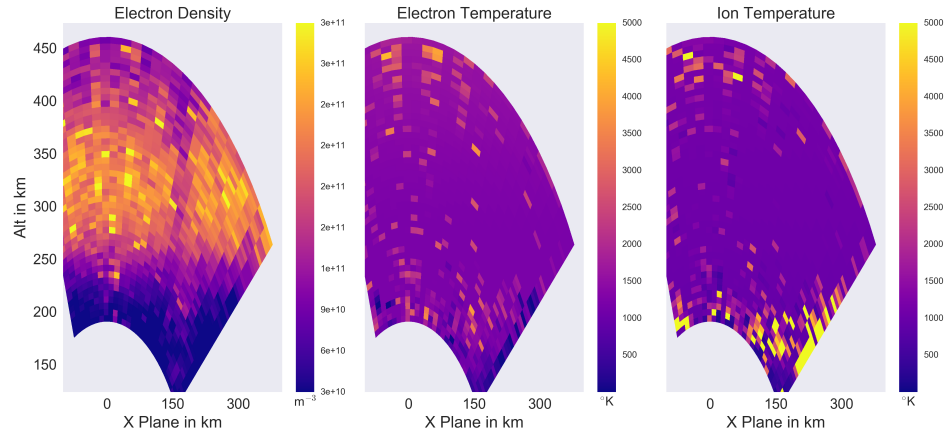


**Figure 15.** Fitted Plasma Parameters at  $t = 480$  s with 60 second integration.

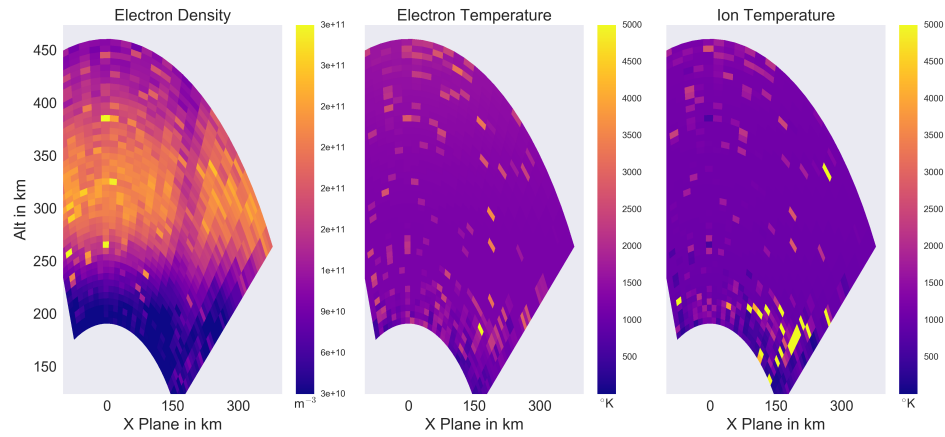


**Figure 16.** Fitted Plasma Parameters at  $t = 480$  s with 240 second integration.

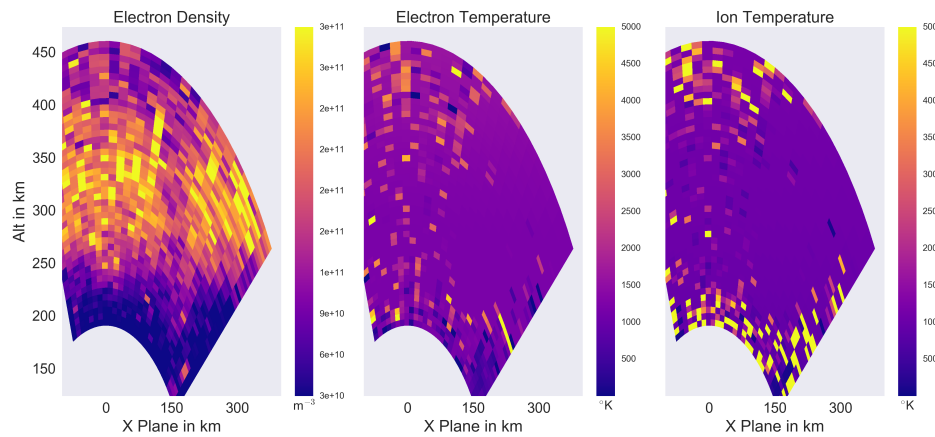


**Figure 17.** Fitted Plasma Parameters at  $t = 480$  s with 15 second integration.